A General Framework for Pearlescent Materials

IBÓN GUILLÉN, Universidad de Zaragoza - I3A
JULIO MARCO, Universidad de Zaragoza - I3A
DIEGO GUTIERREZ, Universidad de Zaragoza - I3A
WENZEL JAKOB, École Polytechnique Fédérale de Lausanne
ADRIAN JARABO, Universidad de Zaragoza - I3A and Centro Universitario de la Defensa Zaragoza

Fig. 1. We present a general model for pearlescent materials, which simulates their complex optical behavior. Our model reproduces and parameterizes the key physical attributes produced by the manufacturing process of such materials, and the resulting reflectance functions closely agree with measured data. In this image, we show how changing a single parameter in each pair of bottles (as indicated by the brackets) leads to large, difficult-to-predict changes in appearance. From left to right, the changed parameters are: a) platelet density variation; b) substrate composition; c) deviation of the platelet normal distribution; d) deviation of the substrate thickness. The rightmost jar shows the values of our model parameters for its particular material. Please refer to Table A3 for a complete description of all the materials.

The unique and visually mesmerizing appearance of pearlescent materials has made them an indispensable ingredient in a diverse array of applications including packaging, ceramics, printing, and cosmetics. In contrast to their natural counterparts, such synthetic examples of pearlescence are created by dispersing microscopic interference pigments within a dielectric resin. The resulting space of materials comprises an enormous range of different phenomena ranging from smooth lustrous appearance reminiscent of pearl to highly directional metallic gloss, along with a gradual change in color that depends on the angle of observation and illumination. All of these properties arise due to a complex optical process involving multiple scattering from platelets characterized by wave-optical interference. This article introduces a flexible model for simulating the optics of such pearlescent 3D microstructures. Following a thorough review of the properties of currently used pigments and manufacturing-related effects that influence pearlescence, we propose a new model which expands the range of appearance that can be represented, and closely reproduces the behavior of measured materials, as we show in our comparisons. Using our model, we conduct a systematic study of the parameter space and its relationship to different aspects of pearlescent appearance. We observe that several previously ignored parameters have a substantial impact on the material's optical behavior, including the multi-layered nature of modern interference pigments, correlations in the orientation of pigment particles, and variability in their properties (e.g. thickness). The utility of a general model for pearlescence extends far beyond computer graphics: inverse and differentiable approaches to rendering are increasingly used to disentangle the physics of scattering from real-world observations. Our approach could inform such reconstructions to enable the predictive design of tailored pearlescent materials.

CCS Concepts: • **Computing methodologies** → **Rendering**.

Additional Key Words and Phrases: Material appearance, iridescence

1 INTRODUCTION

Pearlescent materials have gained significant attention over the last decades. Despite being composed of relatively cheap materials, they are designed to exhibit a wide variety of attractive appearance, with a lustrous shade, metallic-like soft gloss, and vivid goniochromatic effects. These rich visual features have made these materials popular in the cosmetic industry since the 17th century [Pfaff and Becker 2012], with a wide adoption in the 50's. More recently, the car and packaging industries have adopted them to create special-effect, luxurious looks [Maile et al. 2005]. In addition, they are currently starting to impact other fields such as clothing [Mahltig et al. 2017], or ink printing [Pjanic and Hersch 2015].

Authors' addresses: Ibón Guillén, Universidad de Zaragoza - I3A, ibon@unizar.es; Julio Marco, Universidad de Zaragoza - I3A, juliom@unizar.es; Diego Gutierrez, Universidad de Zaragoza - I3A, diegog@unizar.es; Wenzel Jakob, École Polytechnique Fédérale de Lausanne, wenzel.jakob@epfl.ch; Adrian Jarabo, Universidad de Zaragoza - I3A and Centro Universitario de la Defensa Zaragoza, ajarabo@unizar.es.

The intricate appearance of pearlescent materials is obtained by leveraging the optical properties of special pigments embedded into a hosting medium, called the container. These special pigments consist of oriented microscopic platelets with a layered structure of nanoscopic thickness. Given their scale and planar geometry, as light scatters within the platelets it experiences interference effects. This results in highly directional and vivid colors.

Simulating the appearance of pearlescent materials is a complex task. A complete model needs to take into account the volumetric nature of such materials, including light transport inside the container, as well as volumetric scattering and complex anisotropic, interference-based light scattering involving the platelets. On top of that, the final appearance is highly dependent on the particular composition and structure of the platelets in the material, as well as their macroscopic orientation and distribution. This results in a highly non-linear appearance, which is difficult to predict and model. Figure 1 shows several examples of these strong, non-linear effects that arise by changing a single parameter in a pearlescent material.

Some existing works have proposed models of pearlescent materials, targeting the particular case of car paints [Ergun et al. 2016; Ershov et al. 2001]. However, these models are rather limited in the range of appearance that can be simulated, since they are based on many simplifying assumptions that reduce their parameter space.

In this work, we present a general model for pearlescent materials. We review the existing literature from manufacturers (e.g., [Mahltig et al. 2017; Maile et al. 2005; Maile and Reynders 2003; Pfaff and Reynders 1999]), which allows us to extract meaningful parameters that define the structure and optical properties of such materials. From this analysis, we develop a general radiative model for representing these materials, including a rigorous mathematical model for light scattering in platelets. Based on this model, we further analyze the gamut and behavior of the goniochromatic appearance of pearlescent materials, as their defining parameters change. We found that the angular effect of chromaticity lies on a narrow manifold, whose shape is directly related to the platelet reflectivity (gloss component) and transmittance (diffuse component). Furthermore, our analysis helps establish connections between low-level manufacturing parameters, and their effect on the material appearance.

We compare against real-world data, and show that our model reproduces ground-truth reflectance measurements more faithfully than prior work. Our model is fully spectral to avoid spectral aliasing, stochastic, and easy to integrate in any Monte Carlo renderer with multispectral support. Beyond the field of computer graphics, our work has potential applications in manufacturing: for instance, it might allow inverse methods to optimize appearance from actual fabrication parameters. This in turn has strong potential to enable predictive design of pearlescent materials in industries such as cosmetics, fine printing, effect paints, or packaging.

2 RELATED WORK

Volumetric Materials. Light transport simulations involving volumetric materials typically build on the radiative transfer equation (RTE) [Chandrasekhar 2013], and its generalizations to anisotropic [Jakob et al. 2010] and correlated [Bitterli et al. 2018; Jarabo et al. 2018] media. Anisotropy in volumetric materials is generally modeled using *microflakes* [Heitz et al. 2015; Zhao et al. 2011]. Wave effects such as polarization [Jarabo and Arellano 2018], or speckle [Bar et al. 2019] have also been incorporated into the radiative transfer framework. Our work models pearlescent polymers as a stack of dielectric layers that are each filled with an anisotropic medium that reproduces the behavior of the container and platelets.

Stratified Materials. The complexity of real-world appearance is in part due to its stratified (layered) structure. Hanrahan and Krueger [1993] proposed a general model for layered materials, based on expensive subsurface scattering computations, ignoring rough dielectric boundaries. Donner and Jensen [2005] developed a significantly faster solution leveraging the diffusion approximation of light transport. Stam [2001] generalized Hanrahan and Krueger's work taking into account rough boundaries, in the context of skin rendering. A later model [Jakob et al. 2014a] proposed to handle arbitrary layer stacks using the adding-doubling method, handling all-frequency isotropic scattering. Zeltner and Jakob [2018] then generalized this work to include anisotropic scattering. All of these methods require expensive precomputation. Other works [Belcour 2018; Guo et al. 2016; Weidlich and Wilkie 2007; Yamaguchi et al. 2019] proposed faster analytical solutions by stacking a set of BSDFs encoding the different effects of light transport. However, they rely on some approximations, and impose hard limitations on the type of materials that can be handled. Guo et al. [2018b] introduced an efficient Monte Carlo strategy for sampling the effective BRDF of a layered material that we also use in our work. Our work is based on precise modeling of light transport in stratified, pearlescent materials.

Wave-Based Scattering. Several works take into account relevant wave effects including diffraction-aware BSDFs [Dong et al. 2015; Falster et al. 2020; Holzschuch and Pacanowski 2017; Stam 1999; Toisoul and Ghosh 2017; Werner et al. 2017; Yan et al. 2018], phase functions (based on Mie scattering) [Frisvad et al. 2007; Sadeghi et al. 2012], or goniochromatic patterns due to birefringence [Steinberg 2019]. Goniochromatic effects due to electromagnetic interference have been simulated for single-layer thin coatings [Belcour and Barla 2017; Gondek et al. 1994; Granier and Heidrich 2003; Kneiphof et al. 2019; Smits and Meyer 1992; Sun and Wang 2008], and multiple-layer thin coatings [Hirayama et al. 2001; Sun 2006]. In our work we model the scattering in individual iridescent platelets by using multiple thin coatings; however, as opposed to the works by Sun et al. and Hirayama et al., we compute the exact reflectance and transmittance at run-time, without any precomputation.

Pearlescent Materials. The work of Gondek et al. [1994] is the first to consider the problem of rendering pearlescent materials. This technique used a tabulated precomputation of the appearance of such materials by brute-force simulation over explicit geometry. Rump et al. [2008] and Kim et al. [2010] used a data-driven representation of pearlescent paints based on bidirectional texture functions (BTF), limited to the reproduction of previously measured samples. Guo et al. [2018a] assumed plastic strata as a composite of coated discrete microfacets, omitting important effects like the

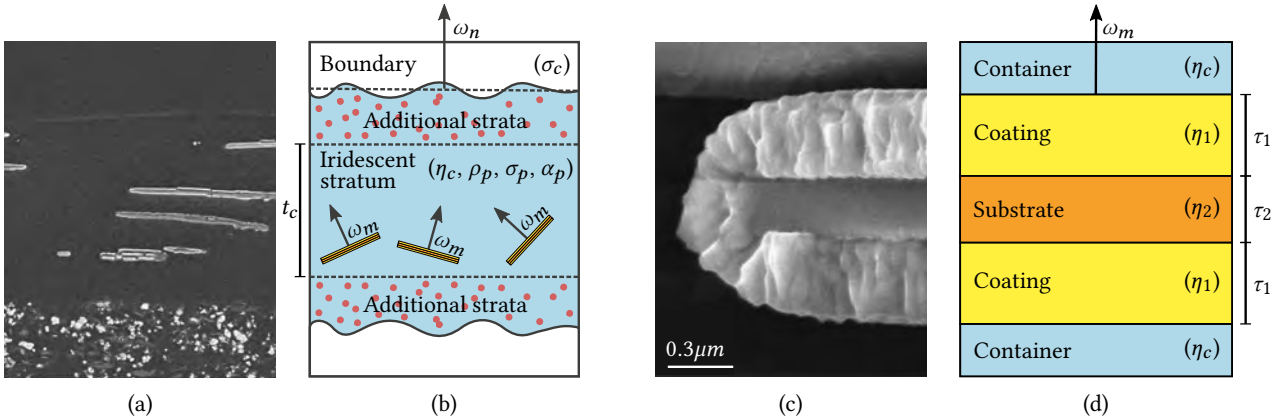

Fig. 2. **(a)** Electronic microscopic capture of a manufactured plastic, where the embedded iridescent platelets can be observed. **(b)** Illustrative scheme of our model for pearlescent materials, where the layers and platelets are shown, along with their key parameters. Note that our model supports optional additional strata, which might also be pearlescent. **(c)** Electronic microscopic capture of a silica platelet. **(d)** Schematic view of our basic platelet model. Our model generalizes to include an arbitrary number of parallel coating layers, bounded at the top and bottom by the container media (see Figure 3 for more complex platelet structures). Image a) from: [Rösler et al. 2008]; used with permission. Image c) from: [Maile et al. 2005]; used with permission.

global color shift caused by multiply scattered light. Volumetric models [Ergun et al. 2016; Ershov et al. 2001] include single and multiply scattered light in a radiative framework, but require expensive precomputations, and impose assumptions on the distribution of the iridescent platelets and their composition, focusing on the particular pigments used in car paint. In contrast, we develop a general model that requires no precomputation, allows spectral rendering with minimal overhead, lifts most assumptions regarding the thickness of the platelets, and supports arbitrary platelets orientation including anisotropy and rotated platelets. Moreover, we show that our model provides a better match to real-world captured materials.

Several works in the optics community have characterized the directionally-varying reflectance gamut of pearlescent materials in terms of the incident and view angles, but they did not consider links to the underlying physical properties of the pigments. For instance, Medina [2008] analyzed the spectral goniochromaticity of pearlescent materials by using principal component analysis. Ferrero et al. [2014] measured a set of real-world pearlescent car paints; later, Ferrero et al. [2016] extended this to diffraction-based pigments. We rely on their measured materials as a source of ground-truth reflectance data to conduct a comparative evaluation of several models in Section 6.1.

3 PEARLESCENT MATERIALS

In contrast to other diffractive effects [Cuypers et al. 2012; Stam 1999], or thin-film iridescence [Belcour and Barla 2017], pearlescence is the result of both volumetric absorption and electromagnetic interference effects in small layered, platelet-shaped structures with an average thickness of just a few nanometers. These *platelets* are uniformly distributed inside a base medium called the *container*, which creates the illusion of increased depth [Maile et al. 2005]. Figure 2 (a) shows a scanning electron microscope (SEM) capture of the cross-section of a manufactured pearlescent plastic, along with a magnified view of a single platelet (c).

Platelets. Platelets are made of transparent or semitransparent materials. They consist of a single optically homogeneous thin layer (*substrate-free* platelets), or form layered structures (*substrate-based* platelets). Substrate-free platelets have an optical thickness in the order of one fourth of the wavelenght of visible light. They can be made up of single crystals, such as bismuth oxychloride (BiOCl), or polycrystalline platelets, made e.g. of titanium dioxide (TiO_2). However, these pigments are not commonly used in practice given the difficulty of crystallizing as thin platelets.

Substrate-based platelets, on the other hand, are much easier to fabricate. The substrate is a thin layer, typically between 100 and 1000 nm, made of a material with a low index of refraction. Approximately 98% of all fabricated substrates are transparent mica [Maile and Reynders 2003]. Other refractive materials with a higher index of refraction can be precipitated onto it, forming a coating layer around the substrate. The large difference in index of refraction between the substrate and the coating layer maximizes the desired interference effects. The most commonly used material for precipitation is titanium dioxide (TiO_2), which is almost transparent; this maximizes the color resulting from iridescence, while having minimum light loss. Some particular effects require the application of several levels of coating over the substrate [Steinbach and Schmidt 2010]. Please refer to Maile's work [2005] for more details about their chemical composition and fabrication processes.

Container. The container is usually made of a cheap thermoplastic resin like polyethylene terephthalate (PET) in the case of plastics, or acrylic polyurethane for car paints. Among other mechanical reasons, these materials are chosen to maximize transparency with negligible absorption and scattering. The container may also be colored by adding wavelength-dependent absorbing dyes. This container is mixed with the platelets (which in general represent a small fraction of the total composite [Wang et al. 2014]). To achieve controllable and reproducible appearance, the thickness distribution of the platelets in the container must be narrow. During fabrication,

Table 1. Common symbols and units used throughout the paper.

η	Complex refractive index
λ	Wavelength [nm]
ω_i, ω_o	Incident and outgoing directions
Σ_t, Σ_s	Extinction and scattering coefficients [m^{-1}]
$f_p(\omega_i \to \omega_o)$	Phase function [sr^{-1}]
ω_m	Platelet normal
η_j	Refraction index of platelet j-th coating layer
τ_j	Thickness of platelet j-th coating layer [nm]
η_s	Refraction index of platelet substrate
τ_s	Thickness of platelet substrate [nm]
$\mathcal{R}(\omega_i), \mathcal{T}(\omega_i)$	Platelet reflectivity (3) and transmissivity (4) functions
ρ_p	Density of a iridescent stratum [m^{-3}]
C_p	Fraction of stratum volume occupied by platelets [%]
σ_p	Bulk platelet cross-section [m^{-2}]
$D_{\omega_i}(\omega_m)$	Distribution of visible platelet normal directions
$\sigma_p^x, \sigma_p^y, \sigma_p^z$	Platelet mean normal deviation in canonical directions
$D(\tau_{p,s})$	Distribution of platelet substrate thicknesses
$\gamma_{p,s}$	Thickness std. deviation of platelet substrate [nm]
$\widehat{\mathcal{R}}(\omega_i), \widehat{\mathcal{T}}(\omega_i)$	Bulk platelet reflectance and transmittance functions (15)
α_p	Bulk platelet albedo
ω_n	Container surface normal
η_c	Refraction index of container material
t_c	Thickness of the container [μm]
α_c	Albedo of container material
σ_c	Roughness of container interface

the platelets get oriented roughly in parallel to the surface of the container as a result of stretching. However, this orientation can be altered during molding [Culeron et al. 2016], yielding a broader normal distribution that alters the brightness of the surface [Seubert et al. 2016].

In the following, we first describe our model of light scattering by individual iridescent platelets (Section 4). The scattering function derived from such model will then be incorporated into our global model for pearlescent materials (Section 5).

4 MODELING SCATTERING BY IRIDESCENT PLATELETS

Our platelet model consists of a stack of locally planar, parallel thin layers with normal ω_m (as seen in Figure 2d). Given that platelets are extremely thin, with thickness varying between 100 and 1000 nm [Maile and Reynders 2003], we assume that they are infinite in the horizontal domain. In addition, we build on the far-field approximation, assuming an incoming planar field on the platelet. Each layer j in a platelet is characterized by its thickness τ_j and a wavelength-dependent complex index of refraction $\eta_j(\lambda)$. For convenience, Table 1 summarizes the symbols and notation used throughout the paper.

Scattering function. The scattering function $\mathcal{F}_p(\omega_i, \omega_o, \lambda)$ of a platelet for wavelength λ is defined as the sum of two Dirac delta functions for reflection and transmittance

$$\mathcal{F}_p(\omega_i, \omega_o, \lambda) = \mathcal{R}(\omega_i, \lambda)\, \frac{\delta(\omega_m - \omega_h)}{4|\omega_h \cdot \omega_i|} + \mathcal{T}(\omega_i, \lambda)\, \delta(\omega_i - \omega_o), \quad (1)$$

where $\omega_h = (\omega_i + \omega_o)/|\omega_i + \omega_o|$ is the half vector, $|\cdot|$ represents the absolute dot product, and $\mathcal{R}(\omega_i, \lambda)$ and $\mathcal{T}(\omega_i, \lambda)$ quantify the proportions of the reflected and transmitted light in the platelet, respectively. The delta function $\delta(\omega_i - \omega_o)$ in the transmittance is consequence of the symmetric parallel structure of the platelet, which reverts the effect of the Snell's law until it cancels out at light leaving the platelet. Given the thinness of the platelet layers, we need to take into account wave optics for computing Equation (1). For substrate-free platelets, $\mathcal{R}(\omega_i, \lambda)$ and $\mathcal{T}(\omega_i, \lambda)$ can be computed using Airy summation, as done for thin-layer interference models [Belcour and Barla 2017; Smits and Meyer 1992]. However, substrate-based platelets require a significantly more complex model, which we describe in the following subsection.

4.1 Scattering in substrate-based platelets

In the general case of substrate-based platelets, one or more coating layers surround the substrate, resulting in an N-layered structure (see Figure 2d). For a given direction ω_i and wavelength λ, the reflectivity $\mathcal{R}(\omega_i, \lambda)$ and transmissivity $\mathcal{T}(\omega_i, \lambda)$ of the N-layered platelet in Equation (1) are given by a plane-parallel solution of Maxwell's equations, tracking the influence of each layer on both amplitude and phase in order to express the effects of interreflection in terms of constructive and destructive interference. This solution can be efficiently evaluated using the *transfer matrix method* [Born and Wolf 1999; Yeh 1988]. The response of the layered structure for each polarization component of the electromagnetic field is given by the 2×2 *response matrix* M as

$$M = \prod_{j=1}^{N} M_j = \begin{pmatrix} m_{11} & m_{12} \\ m_{21} & m_{22} \end{pmatrix},$$

where M_j represents the individual response of each layer j. It is defined as (see [Born and Wolf 1999, Ch.1.6.2] for details)

$$M_j = \begin{pmatrix} \cos\Delta\phi_j & -\frac{i}{q_j}\sin\Delta\phi_j \\ -i\, q_j \sin\Delta\phi_j & \cos\Delta\phi_j \end{pmatrix}, \quad (2)$$

where $\Delta\phi_j = 2\pi\lambda^{-1}\eta_j(\lambda)\,\tau_j \cos\theta_j$ is the phase shift of the incident light inside the layer, and θ_j is the transmission angle. The matrix M_j is different for each polarization component, with the tilted admittance q_j taking values $q_{\perp,j} = \eta_j(\lambda)\cos\theta_j$ and $q_{\parallel,j} = \cos\theta_j / \eta_j(\lambda)$ for the perpendicular and parallel polarization components, respectively. The value of $\cos\theta_j$ for each layer depends on the corresponding cosine of the previous layer, following Snell's law, with $\cos\theta_0 = \omega_m \cdot \omega_i$. To take into account the boundaries with the container, we consider two additional layers (top and bottom, see Figure 2) with $\eta_0 = \eta_{N+1} = \eta_c$. Given the symmetry of index of refraction changes in the layered structure, we have $\cos\theta_{N+1} = -\cos\theta_0$.

From the elements of the response matrix M, we obtain the complex reflection and transmission coefficients as

$$r = \frac{(m_{11} + m_{12}\, q_c)\, q_c + (m_{21} + m_{22}\, q_c)}{(m_{11} + m_{12}\, q_c)\, q_c - (m_{21} + m_{22}\, q_c)},$$

$$t = \frac{2\, q_c}{(m_{11} + m_{12}\, q_c)\, q_c - (m_{21} + m_{22}\, q_c)},$$

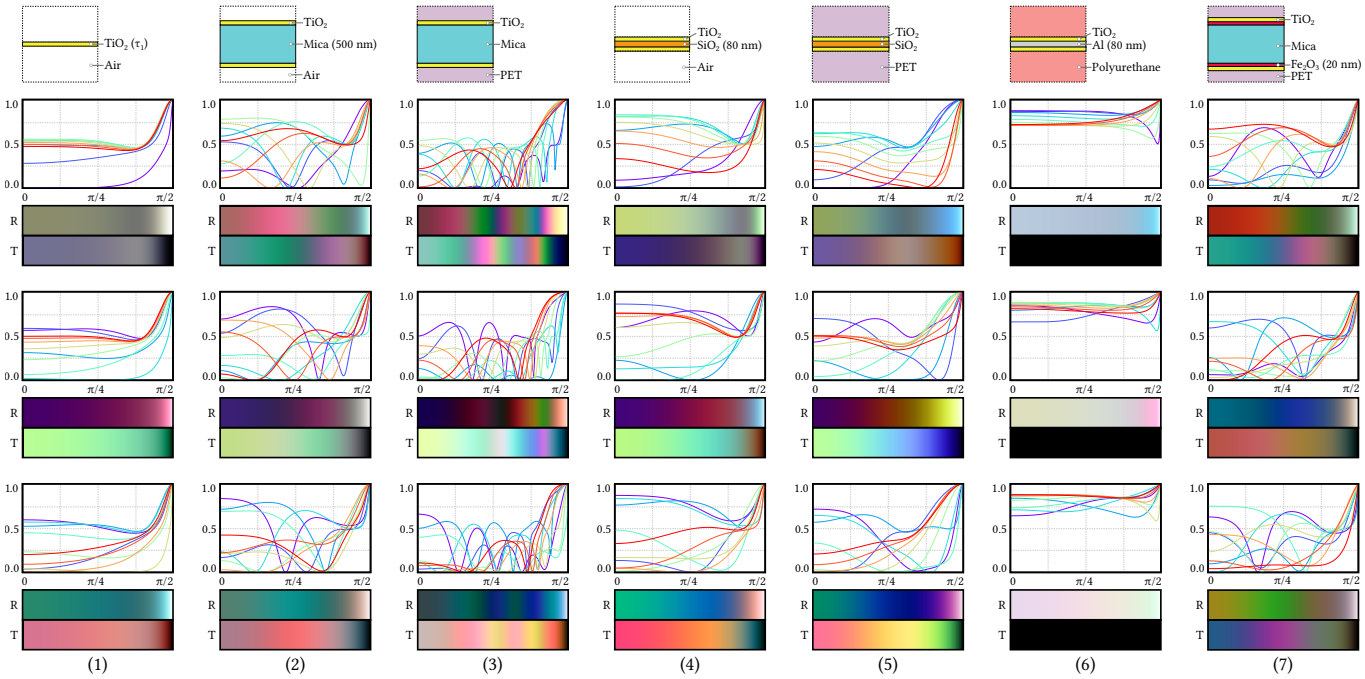

Fig. 3. Scattering functions for different platelets. **(1)** Substrate-free platelet made of a single TiO_2 layer; Equation (1) can be solved as an Airy summation. **(2)** Mica substrate coated with TiO_2. **(3)** Mica substrate coated with TiO_2, in a PET container. **(4)** Silica (SiO_2) substrate coated with TiO_2. **(5)**Silica (SiO_2) substrate coated with TiO_2, in a PET container. **(6)** Metallic (aluminum) substrate coated with TiO_2, in a PET container. **(7)** Mica substrate coated with ferric oxide (Fe_2O_3), and TiO_2, in a PET container. The mica substrates are 500 nm thick; silica and aluminum substrates are 80 nm; ferric oxide is 20 nm. The thickness of the TiO_2 coating layers varies in each column, from 60 nm (top), 100 (middle), and 140 nm (bottom). For each resulting platelet, the plots show the directional reflectance with respect to the incident angle for ten uniformly distributed wavelengths within the visible spectrum (360-830 nm, top plots), while the color gradients represent the resulting directional reflectance and transmittance in sRGB under a D65 illuminant.

where q_c refers to the tilted admittance of the container. Both M and q_c have to be obtained for the perpendicular ($r_\perp$, $t_\perp$) and parallel ($r_\parallel$, $t_\parallel$) components of the field.

Finally, assuming unpolarized incident light, we compute the total reflectivity and transmissivity of the layered structure as

$$\mathcal{R}(\omega_i, \lambda) = \frac{1}{2}\left(|r_\perp|^2 + |r_\parallel|^2\right), \tag{3}$$

$$\mathcal{T}(\omega_i, \lambda) = \frac{1}{2}\left(|t_\perp|^2 + |t_\parallel|^2\right). \tag{4}$$

4.2 Analysis

Having presented the platelet, we showcase the complex nonlinear dependence of their reflectance properties on the layer structure before moving on to the full volumetric model in Section 5.

Figure 3 shows the scattering behavior of different platelets using our model described in Section 4.1. We take titanium dioxide (TiO_2) as the main coating material since it is one of the most commonly used. All the structures shown (columns) are used in real applications such as cosmetics, plastic manufacturing, or car paint [Pfaff and Reynders 1999; Seubert et al. 2016; Shiomi et al. 2008]. The only exception is the first column, which presents a simple substrate-free, TiO_2 platelet included for illustration purposes. In particular, each column shows the following:

(1) Substrate-free, TiO_2 platelet
(2) Mica substrate coated with TiO_2
(3) Mica substrate coated with TiO_2, in a PET container
(4) Silica (SiO_2) substrate coated with TiO_2
(5) Silica (SiO_2) substrate coated with TiO_2, in a PET container
(6) Aluminum substrate coated with TiO_2, in a polyurethane container
(7) Mica substrate coated with ferric oxide (Fe_2O_3) and TiO_2, in a PET container

The thickness of the TiO_2 layer increases from top to bottom in each column. Each row shows the directional reflectance with respect to the incident angle for ten uniformly distributed wavelengths (360-830 nm, top plots), as well as the resulting directional reflectance and transmittance in sRGB under a D65 illuminant. We do not plot the directional transmittance to avoid cluttering the plots; since mica and silica have a negligible absorption, transmittance curves are symmetric to the reflectance curves. Introducing aluminium and ferric oxide in the last two platelets adds some absorption, which breaks this symmetry.

This analysis reveals that multiple parameters have a large impact on the final appearance of the material. First, the effect of the coating thickness is very relevant. Second, the substrate material also affects the platelet's scattering, even for the same coating thickness (e.g., fifth and sixth columns): Transparent substrates such as mica or SiO_2 yield a strong transmittance while highly absorbing substrates

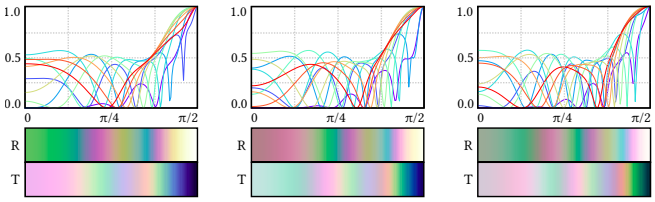

Fig. 4. Varying the substrate thickness leads to changes in platelet appearance. From left to right, mica substrate with thickness $\tau_s = 400$ nm, 500 nm and 600 nm, respectively (fixed TiO_2 coating of $\tau_1 = 60$ nm). Top: directional, wavelength-dependent reflectance curves. Bottom: reflectance and transmittance in sRGB under a D65 illuminant (similar to Figure 3).

such as aluminum are opaque. Third, the reflectance and transmittance gradients illustrate the rich variations in appearance of these materials, resulting from the combination of both. And fourth, the container also plays an important role in the final appearance (e.g., second and third columns; plastics generally use PET as container, while powder-based cosmetics use no container).

For artificial substrates such as SiO_2, thickness can be carefully controlled within an error of ±5 nm, and it is usually set to 80 nm. In contrast, for natural mica substrates τ_s is very difficult to control, resulting in a considerable thickness variation within the same material. Figure 4 illustrates the effect of these variations on the reflectance and transmittance.

5 LIGHT TRANSPORT IN PEARLESCENT MATERIALS

In this section we show how to incorporate the scattering function for a single platelet (Section 4) into our global model for pearlescent materials, and we conclude it with a discussion of important implementation-level details. As described in Section 3, pearlescent materials can be composed of a single or multiple strata (Figure 2b illustrates the simple case of a single-stratum material). The appearance of these materials is the result of the volumetric radiative transport in the container and the platelets of each stratum. The platelets can be assumed to be uncorrelated and randomly distributed throughout their medium [Rösler et al. 2008], so non-exponential radiative transport [Bitterli et al. 2018; Jarabo et al. 2018] does not need to be considered. Furthermore, we assume that wave-optical coherence effects play no role given the comparably large distance and random distribution of lengths between medium interactions.

In contrast to regular radiative transfer, which assumes isotropic spherical particles, pearlescent materials are composed of platelets that break the spherical symmetry assumption of traditional radiative transfer theory. As a consequence, we rely on the anisotropic formulation of the radiative transfer equation (RTE) introduced by Jakob et al. [2010]. This formulation adds directional and positional dependency to all the relevant properties of the media, and couples them directly with the geometry of the scattering particles. In the absence of source terms, which can be removed in pearlescent materials, this framework models the radiance L in direction

$$\omega_o \cdot \nabla L(\omega_o) + \Sigma_t(\omega_o) L(\omega_o) = \Sigma_s(\omega_o) \int_\Omega f_p(\omega_i \rightarrow \omega_o) L_i(\omega_i) d\omega_i, \tag{5}$$

where $\Sigma_t(\omega_o)$ and $\Sigma_s(\omega_o)$ are the directionally-dependent extinction and scattering parameters respectively, Ω is the sphere of directions, $f_p(\omega_i \rightarrow \omega_o)$ is the phase function, and ω_i is the incoming direction. Note that we have omitted the spatial and spectral dimensions for simplicity.

5.1 Modeling optical properties of pearlescent media

The appearance of a pearlescent medium is characterized by $\Sigma_t(\omega_o)$, $\Sigma_s(\omega_o)$, and $f_p(\omega_i \rightarrow \omega_o)$ in Equation (5). These three parameters depend on the optical parameters describing the container, including the presence of absorbing dyes, as well as the mixture of suspended platelets in it. In particular,

$$\Sigma_t = \Sigma_t^{\mathrm{c}} + \sum_{j=1}^{M} \Sigma_t^{\mathrm{p}_j}, \tag{6}$$

$$\Sigma_s = \Sigma_s^{\mathrm{c}} + \sum_{j=1}^{M} \Sigma_s^{\mathrm{p}_j}, \tag{7}$$

$$f_p(\omega_i \rightarrow \omega_o) = \frac{\Sigma_s^{\mathrm{c}}}{\Sigma_s} f_p^{\mathrm{c}}(\omega_i \rightarrow \omega_o) + \sum_{j=1}^{M} \frac{\Sigma_s^{\mathrm{p}_j}}{\Sigma_s} f_p^{\mathrm{p}_j}(\omega_i \rightarrow \omega_o), \tag{8}$$

where we use the superscripts c and p_j to refer to the container and platelet j respectively.

Container. To emphasize the iridescent properties of the material, the container is typically chosen to have minimum scattering, exhibiting a mostly transparent appearance. Therefore, we can assume negligible scattering, so that their optical properties are defined only by their complex index of refraction (IOR) η_{c}. The base container material is almost perfectly transparent, leading to a very small imaginary part in η_{c}. However, it is common to add some colouring dye. Its extinction, scattering, and phase function (Σ_t^{d}, Σ_s^{d}, and $f_p^{\mathrm{d}}(\omega_i \rightarrow \omega_o)$, respectively) can be computed using Lorentz-Mie theory [Frisvad et al. 2007], parameterized by the concentration of pigment particles ρ_{d}, the particle size distribution $D(r_{\mathrm{d}})$, and the complex index of refraction $\eta_{\mathrm{d}}(\lambda)$. In summary, the optical parameters of the container for a given wavelength λ are

$$\Sigma_t^{\mathrm{c}} = 4\pi \,\mathrm{Im}\left(\eta_{\mathrm{d}}(\lambda)\right) \lambda^{-1} + \Sigma_t^{\mathrm{d}}, \tag{9}$$

$$\Sigma_s^{\mathrm{c}} = \Sigma_s^{\mathrm{d}}, \tag{10}$$

$$f_p^{\mathrm{c}}(\omega_i \rightarrow \omega_o) = f_p^{\mathrm{d}}(\omega_i \rightarrow \omega_o), \tag{11}$$

where the first term in Equation (9) is direct consequence of the Beer-Lambert law. Note that these optical parameters do not have angular dependence.

Platelet stratum. The global optical properties of the platelet stratum are determined by the density of platelets ρ_{p}, their projected area $\sigma_{\mathrm{p}}(\omega_i)$ in direction ω_i, and the directional distribution of their

normals $D(\omega_m)$. These parameters define the extinction and scattering coefficients as

$$\Sigma_t^{\mathrm{p}}(\omega_i) = \rho_{\mathrm{p}}\sigma_{\mathrm{p}}(\omega_i), \tag{12}$$

$$\Sigma_s^{\mathrm{p}}(\omega_i) = \alpha_{\mathrm{p}}(\omega_i)\rho_{\mathrm{p}}\sigma_{\mathrm{p}}(\omega_i), \tag{13}$$

where $\sigma_{\mathrm{p}}(\omega_i) = \int_\Omega \langle \omega_m, \omega_i \rangle D(\omega_m) d\omega_m$ [Jakob et al. 2010], with $\langle , \rangle$ the clamped dot product, and $\alpha_{\mathrm{p}}(\omega_i)$ the scattering albedo of the platelets. For a large number of real-world pearlescent platelets the absorption can be considered negligible, therefore $\alpha_{\mathrm{p}}(\omega_i) = 1$. We parameterize the density of platelets as the fraction of platelets with respect to the total volume $C_{\mathrm{p}} = \rho_{\mathrm{p}} V_{\mathrm{p}}$, with V_{p} the average volume of the platelets. We set $V_{\mathrm{p}} = 400\mu m^3$, based on SEM measurements [Maile et al. 2005]. In addition, the thickness of the platelets substrate $\tau_{\mathrm{p,s}}$ might vary significantly (where s indicates the substrate), especially in natural substrates: We model this variability by using a substrate thickness distribution function $D(\tau_{\mathrm{p,s}})$. On the other hand, the thickness of the coating layers can be carefully controlled given the chemical processes involved in coating [Maile et al. 2005]. This results into minimal variations on the platelet's coating thicknesses.

Since $D(\tau_{\mathrm{p,s}})$ and $D(\omega_m)$ are uncorrelated, and using Equation (1) as the scattering function for an individual platelet, we can generalize the derivations by Heitz et al. [2015, Eq. (5)] and compute the phase function of the platelets' substrate as

$$f_p^{\mathrm{p}} = \int_0^\infty \int_\Omega \mathcal{F}_{\mathrm{p}}(\omega_i, \omega_o | \omega_m, \tau_{\mathrm{p,s}}) D(\tau_{\mathrm{p,s}}) D_{\omega_i}(\omega_m) d\omega_m \, d\tau_{\mathrm{p,s}} \tag{14}$$

$$= \frac{D(\omega_m)}{4\,\sigma_{\mathrm{p}}(\omega_i)} \overbrace{\int_0^\infty \mathcal{R}(\omega_i | \tau_{\mathrm{p,s}}) D(\tau_{\mathrm{p,s}}) d\tau_{\mathrm{p,s}}}^{\widehat{\mathcal{R}}(\omega_i)} \tag{15}$$

$$+ \delta(\omega_i - \omega_o) \underbrace{\int_0^\infty \int_\Omega \mathcal{T}(\omega_i | \omega_m, \tau_{\mathrm{p,s}}) D(\tau_{\mathrm{p,s}}) D_{\omega_i}(\omega_m) d\omega_m \, d\tau_{\mathrm{p,s}}}_{\widehat{\mathcal{T}}(\omega_i)}$$

where $D_{\omega_i}(\omega_m) = \frac{D(\omega_m)\langle \omega_m, \omega_i \rangle}{\sigma_{\mathrm{p}}(\omega_i)}$ is the distribution of visible normals; we parameterize $\mathcal{F}_{\mathrm{p}}$ given by (1) by the platelet's normal and the substrate thickness. The first term in Equation (15) is equivalent to a phase function based on specular microflakes [Heitz et al. 2015; Jakob et al. 2010], though the $\widehat{\mathcal{R}}(\omega_i)$ directionally varying albedo constitutes a key difference to prior work. The second term $\widehat{\mathcal{T}}(\omega_i)$ models an ideal forward-scattering peak based on a Dirac delta function. In this way, it behaves very similarly to null-scattering [Miller et al. 2019] and effectively reduces the optical density of the medium. However, in contrast to null-scattering, where this delta term is intentionally added to facilitate unbiased sampling of heterogeneous media, it is not fundamentally needed here. Furthermore, the additional sampling decision to choose between reflection and transmission components would add additional variance in a Monte Carlo framework. For this reason, we directly merge the effects of platelet transmission into Equations (12) and (13), which yields an equivalent description that is easier to sample:

$$\Sigma_t^{\mathrm{p}}(\omega_i) = \rho_{\mathrm{p}}\, \sigma_{\mathrm{p}}(\omega_i) \left(1 - \widehat{\mathcal{T}}(\omega_i)\right), \tag{16}$$

$$\Sigma_s^{\mathrm{p}}(\omega_i) = \alpha_{\mathrm{p}}(\omega_i)\, \rho_{\mathrm{p}}\, \sigma_{\mathrm{p}}(\omega_i) \left(1 - \widehat{\mathcal{T}}(\omega_i)\right), \tag{17}$$

$$f_p^{\mathrm{p}}(\omega_i \to \omega_o) = \frac{D(\omega_m)}{4\,\sigma_{\mathrm{p}}(\omega_i)} \widehat{\mathcal{R}}(\omega_i). \tag{18}$$

5.2 Implementation

We implement our model as a BSDF in Mitsuba 2 [Nimier-David et al. 2019], leveraging its native support for spectral rendering. In this section we provide details about the implementation of the different building blocks.

Position-free Monte Carlo. To implement our pearlescent material model, we leverage the generality of the recent position-free approach by Guo et al. [2018b] for rendering stratified materials. This method builds on the assumption that scattering takes place within a small surface region so that lateral effects can be neglected. This enables a simplified parameterization of the path integral formulation in terms of depth and orientation, where the invariance with respect to lateral displacement enables variance reduction through connection strategies such as next event estimation and multiple importance sampling (MIS). Light transport inside the material is computed stochastically in an unbiased manner, explicitly accounting for all interactions involving particles that permeate the interior of layers, as well as smooth or rough interfaces between layers. Finally, it supports arbitrary complexity and does not require the costly precomputation of prior work based on adding-doubling [Ergun et al. 2016; Ershov et al. 2001].

Spectral rendering. Given the strong dependence on wavelength of the iridescent phase functions, using traditional RGB rendering for volumetric scattering might result in strong spectral aliasing. To avoid potential errors on the appearance reproduction, we implement our model in a fully spectral renderer, which fits very well into our stochastic model. We base our implementation on hero wavelength [Wilkie et al. 2014] for efficiently tracking four wavelengths at the same time. The sampling techniques for each wavelength are then combined via multiple importance sampling (MIS). This is crucial for obtaining low spectral variance (see [Wilkie et al. 2014] for details). In order to calculate the wavelength-dependent index of refraction for platelets and container $\eta(\lambda)$, we use a Cauchy polynomial fit from measured η and Abbe numbers V_d (lower values indicate higher chromatic dispersion) for transparent materials such as mica, SiO_2 , or TiO_2 . For absorbing materials such as Fe_2O_3 or aluminum, we resort to tabulated captured data (see Table A1).

Directional distribution. The directional distribution $D(\omega_m)$ of the platelets in pearlescent materials has been previously analyzed by light microscope images or CT scans (e.g., [Kirchner 2009]). It follows a Gaussian angular distribution [Kettler and Richter 1997; Kirchner and Houweling 2009], with standard deviation between 7° and 30°. While by default the mean direction would be equal to the normal of the pearlescent stratum ω_n, the orientation of the platelets can also be changed, as done in metallic paints to achieve complex appearance effects [Seubert et al. 2016]. Gaussian-based

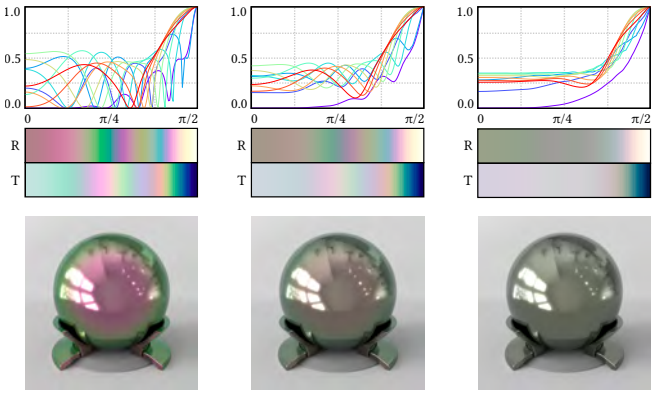

Fig. 5. Response of a mica-substrate platelet with a thickness of $\tau_1 = 500$ nm, and a 60 nm TiO_2 coating, and varying substrate thickness distributions. The leftmost column shows how neglecting the effect of thickness variability [Ergun et al. 2016] may lead to unrealistic appearance. The middle and right columns show results taking into account substrate thickness distributions $D(\tau_{p,s})$ with standard deviation $\gamma_{p,s}$ of 50 and 100 nm, respectively. In this example, interference effects are largely attenuated with increasing $\gamma_{p,s}$, due to loss of coherence of the light reflected within the mica substrate. Note that introducing a stochastic distribution of the thickness does not incur into significant additional variance during rendering (all renders have been done using 4K samples/pixel, 20 mins).

microflake distributions exist [Zhao et al. 2011]; in our work, we employ the roughly equivalent SGGX distribution [Heitz et al. 2015], which models the distribution of normals as an ellipsoid, and allows simpler and more efficient evaluation and sampling of the distribution of visible normals $D_{\omega_i}(\omega_m)$. This model is parameterized by the effective cross section of the particles in each of the orthogonal directions $(\sigma_p^x, \sigma_p^y, \sigma_p^z)$. We set σ_p^z to be the surface area of the platelet, orthogonal to the platelet mean normal $\hat{\omega}_m$ and allow σ_p^x and σ_p^y to be defined independently, thus supporting anisotropic deviation of the platelets. Unless stated otherwise (see Figure 13), the platelet mean normal $\hat{\omega}_m$ in results coincides with the stratum normal ω_n, and we assume an isotropic directional distribution of the platelets (i.e. $\sigma_p^x = \sigma_p^y = \sigma_p^{xy}$).

Substrate thickness distribution. Prior work assumes a constant substrate thickness [Ergun et al. 2016; Ershov et al. 2001]. However, neglecting the effect of thickness variation leads to severe errors in the resulting appearance, as illustrated in Figure 5. Based on measurements of mica-based substrates using an Atomic Force Microscope [Shiomi et al. 2008], we approximate the distribution of substrate thickness $D(\tau_{p,s})$ as a Gaussian distribution with standard deviation $\gamma_{p,s}$. While synthetic substrates such as silica are characterized by narrow distributions [Pfaff 2003], the thickness of mica substrates can range between 100 and 1000 nm, with a mean thickness of 560 nm and a standard deviation of 179 nm [Shiomi et al. 2008].

Platelet stratum extinction coefficient. As defined in Equation (16), the effective extinction coefficient $\Sigma_t^p(\omega_i)$ of an iridescent strata depends on the platelets transmission $\widehat{\mathcal{T}}(\omega_i)$, which in turn is defined not only by the structure of the layers, but also by their distribution of normals $D_{\omega_i}(\omega_m)$ and thicknesses $D(\tau_{p,s})$ (see Equation (15)). Given the complexity of the resulting expression, which involves the evaluation of the transmissivity of the layered structure over both distribution domains, we employ a stochastic evaluation procedure. In particular, when sampling the mean free path or calculating the attenuation, we sample a platelet direction from the distribution of visible normals $D_{\omega_i}(\omega_m)$ (see [Heitz et al. 2015] for details), and a thickness from the Gaussian distribution of $D(\tau_{p,s})$. As mentioned earlier, the main source of variance is due to the strong wavelength dependence of extinction, whereas the variance introduced by the above procedure is insignificant in comparison.

6 ANALYSIS AND EVALUATION

We now turn to evaluation of our method beginning with a comparison to captured reflectance data of real-world iridescent materials. In the second part of this section, we study the behavior of the parameter space in greater detail.

6.1 Comparison with captured data

We compare the results of our model with data from Ferrero and colleagues [2014], who measured a series of pearlescent material samples composed of TiO_2-coated platelets within a Silica substrate, providing discretized measurements of their reflectance field with an angular resolution of 10 degrees. We re-create three materials: *MCS1*, referring to Colorstream® T20-04 WNT Lapis Sunlight manufactured by Merck KGaA; *MCS2*, referring to Colorstream® T20-02 WNT Arctic Fire also manufactured by Merck KGaA; and *BASF1*, a burgundy and green material manufactured by BASF Coatings GmbH.

To populate the parameters of our model, we rely on all the information available from the manufacturers for each material. In particular, the container is made of Polysilazane ($\eta = 1.555$) with a thickness $t_c = 150\ \mu$m and roughness $\sigma_c = 0.01$, and the indices of refraction for TiO_2 and Silica are 2.6142 and 1.4585 respectively (see also Table A1). The remaining parameters are obtained by brute-force optimization within the limits defined by manufacturing parameters reported in the literature [Maile et al. 2005]: coating thickness $\tau_1 \in [60, 170]$ nm, substrate mean thickness $\tau_s \in [80, 500]$ nm, platelets density $C_p \in [3, 13]$%, platelets normal deviation $\sigma_p^{xy} \in [0.01, 0.1]$, and substrate thickness standard deviation $\gamma_s \in [0, 70]$ nm. The fitted parameters for each measured material can be found in Table A2.

We also compare the results achieved with simpler models (Ergun et al.'s [2016], which in turn is based of Ershov's model [2001]), using their available parameters. As observed in Figure 6 and Table 2, our model provides better fits to the measured data, thus allowing us to represent real materials more accurately. Additionally, Figure 7 provides a visual comparison of the resulting distribution of chromaticities. Again, our model (green dots) produces reflectance values that are in closer agreement to ground-truth data than previous models, which tend to deviate significantly in both chromaticity and saturation.

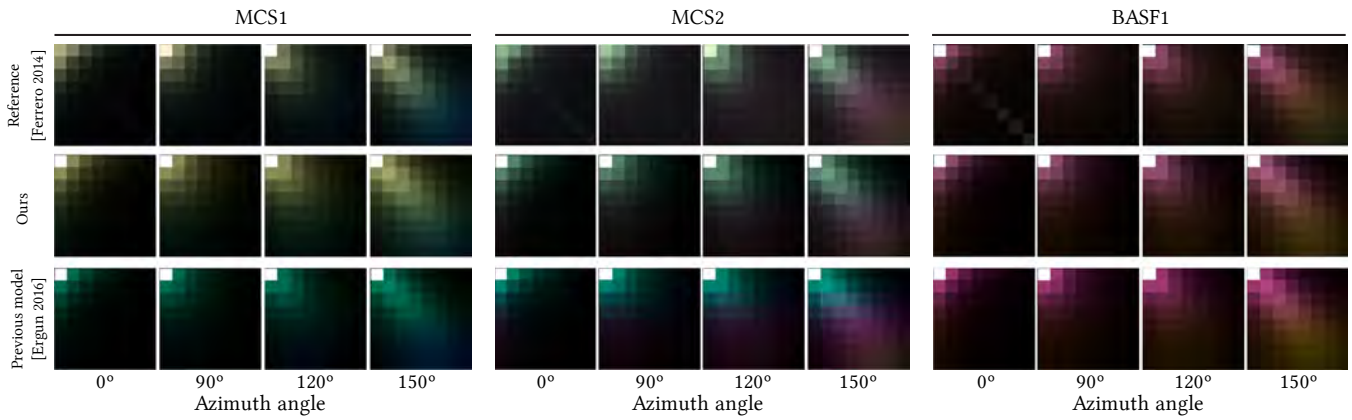

Fig. 6. Comparison of our model with ground-truth measurements [Ferrero et al. 2014] for three different materials: *MCS1*, *MCS2*, and *BASF1* (we keep the same naming as in the source article). The bottom row shows the results using a previous model [Ergun et al. 2016]; our model allows to reproduce real measurements more faithfully (see also Figure 7).

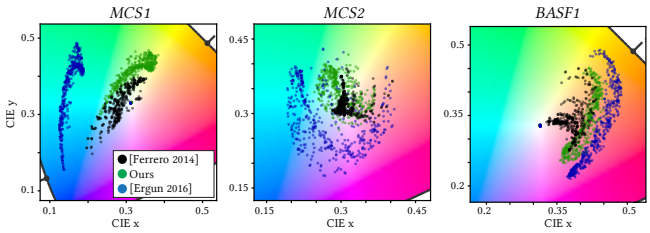

Fig. 7. Chromaticity space of measured materials (black dots) [Ferrero et al. 2014], our model (green), and previous work (blue) [Ergun et al. 2016]. Our model provides a closer match with measured data, with more accurate chromaticities and without excessive saturation.

Table 2. Error comparison of our model and Ergun et al.'s model [2016] for the fits on Ferrero et al.'s [2014] measurements. For each material we report error in CIExy chromaticity space, measured using mean squared error (MSE) and peak signal-to-noise ratio (PSNR).

Material	Model	MSE	PSNR (dB)
MCS1	[Ergun et al. 2016]	0.41400	11.53
	Ours	0.15100	14.74
MCS2	[Ergun et al. 2016]	0.27012	16.61
	Ours	0.08759	21.69
BFS1	[Ergun et al. 2016]	0.25252	17.05
	Ours	0.10579	20.74

6.2 Exploration of the parameter space

The set of optical phenomena that give rise to pearlescent appearance are complex and highly nonlinear: they involve the complex interplay of multiple anisotropic volume scattering, directionally varying interference within platelets, high-frequency spectral variation, interactions with the container, and refraction and internal reflection from layer boundaries. These aspects imply that predictive modeling of pearlescence remains a challenging and computationally intense task.

We performed a large set of simulations using our framework to study the space of pearlescent appearance, as parameterized by our model. We explore the resulting data and discuss our observations in the remainder of this section. We envision that such systematic exploration of material configurations could be a powerful ingredient in the computational design of pearlescence in the future. As explained in the previous sections, our framework supports an arbitrary number of strata. We restrict this analysis to a single-pearlescent-stratum material (such as manufactured plastic containers used by the cosmetic industry) only as a reasonable compromise to illustrate the capabilities of our model, while keeping the number of physical parameters to explore tractable.

We model a material consisting of a pearlescent stratum containing the iridescent platelets, on top of a base stratum (see Figure 8). This material (C1) contains platelets with an 80 nm SiO_2 substrate. The substrate is coated with a TiO_2 layer with a varying thickness τ_1. We include a common PET thermoplastic container with thickness $t_c = 150\ \mu$m, and interface roughness $\sigma_c = 0.01$. These pearlescent strata are applied over a base stratum, such as skin in cosmetic products, or the primer in automotive paints, which reflects light back to the pearlescent material. It thus plays an important role in its final appearance when transmittance is high, resulting in more vivid colors. We model this base stratum and set its diffuse reflectance albedo $\alpha_b = 0.7$.

For our analysis, we use a parameterization based on the half and difference angles (θ_h and θ_d, respectively) [Rusinkiewicz 1998], which avoids redundant information and allows exploring isotropic BSDFs in a simpler 2D domain. Following Burley's intuitive way to visualize materials by means of image slices [Burley 2012], we observe two main goniochromatic effects along the same BRDF (see Figure 9): The first aligns with the difference angle θ_d along the material's gloss component; the second appears on the diffuse reflection β, and is roughly radial with respect to $(\theta_h, \theta_d) = (0, 0)$. Based on these observations, we focus our analysis on the chromaticity

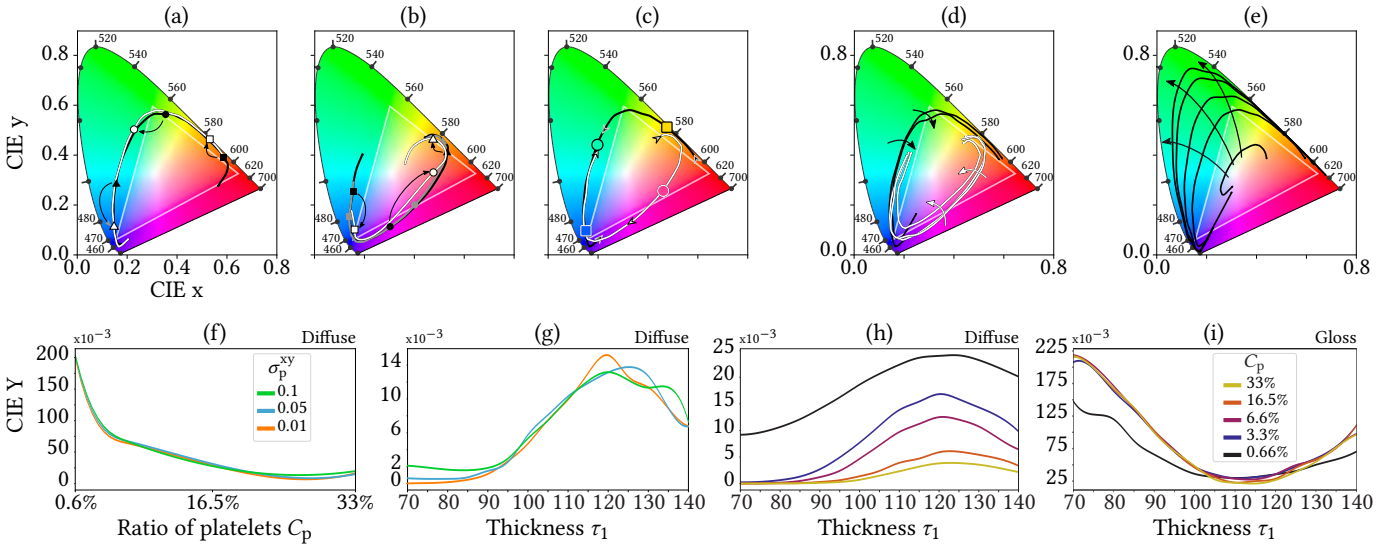

Fig. 10. Effect of the different parameters of material C1 on its appearance (in all the diagrams, the triangle indicates the RGB gamut). **Top row (Chromaticity analysis): (a)** Influence of the TiO_2 coating thickness on the diffuse chromaticity, given a fixed $\sigma_p^{xy} = 0.01$ and $C_p = 3\%$. The two curves shown (black and white), correspond to two different thicknesses; pairs of points on the curves illustrate the changes in diffuse chromaticity as thickness increases. **(b)** Similar diagram for gloss chromaticity, for three curves of different thicknesses. These first two diagrams show how both chromaticities change, but remain within a narrow manifold. **(c)** Diffuse (black) and gloss (white) chromaticities as the thickness of the coating layer increases, for directions close to normal incidence. It can be seen how both components rotate in opposite directions, always showing roughly complementary colors. **(d)** Effect of the deviation of the normal distribution σ_p^{xy} for a fixed platelet density $C_p = 3\%$, showing both the diffuse (black) and gloss (white) components. As the deviation increases (as indicated by the arrows), both components become less saturated. **(e)** Effect of platelet density C_p for a fixed platelet normal deviation $\sigma_p^{xy} = 0.01\%$; as density increases (see arrows), so does saturation. **Bottom row (Luminance analysis):** Diffuse luminance, as a function of density **(f)**, and coating thickness **(g)** for different platelet normal distribution deviations σ_p^{xy}. Diffuse **(h)** and gloss **(i)** luminance as a function of coating thickness τ_1 for different densities.

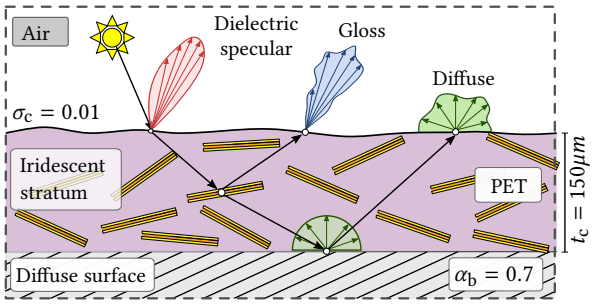

Fig. 8. Schematic view of the material structure used for modeling materials C1 and C2. Both materials consist of an iridescent plastic stratum on top of a base diffuse layer. Note that we use single-stratum material for our analysis to keep the parameter space tractable; our model supports an arbitrary number of layers. We analyze the optical behavior of this pearlescent material, in particular the influence of our model parameters on the goniochromatic diffuse and gloss components, which are in turn affected by the platelet characteristics and the strata below the container.

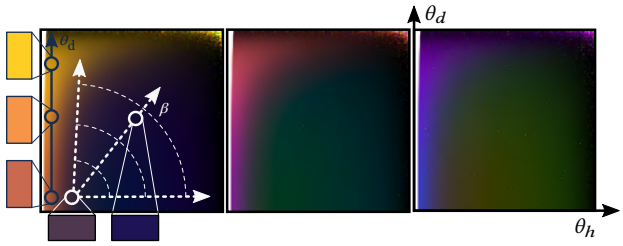

Fig. 9. 2D image slices representations [Burley 2012] of the reflectance of material C1, for three different coating thickness τ_1. Superimposed on the left, we can see the two main axes of goniochromaticity: One axis runs along the difference angle on the specular reflection (black); the second axis β (white) describes variations in diffuse reflection, and is radial from the normal reflection. The dots on top of each of both axes represent the angular location of the samples used in our analysis.

and luminance, by exploring the effect of our model parameters on those two axes.

Chromaticity. Figure 10a illustrates the changes in diffuse chromaticity β, on a CIE xyY diagram as the thickness τ_1 of the platelets' TiO_2 coating increases. We fix the platelet density $C_p = 3\%$ of the total volume, and the deviation to the normal distribution to $\sigma_p^{xy} = 0.1$. It can be seen how the diffuse chromaticity falls in a very narrow manifold, which is mostly outside the sRGB gamut (shown as a superimposed white triangle). Pairs of points on the different curves indicate equal diffuse coordinates, showing how the diffuse component travels along the manifold as τ_1 increases. Figure 10b shows a similar behavior for gloss chromaticity, except that the diffuse

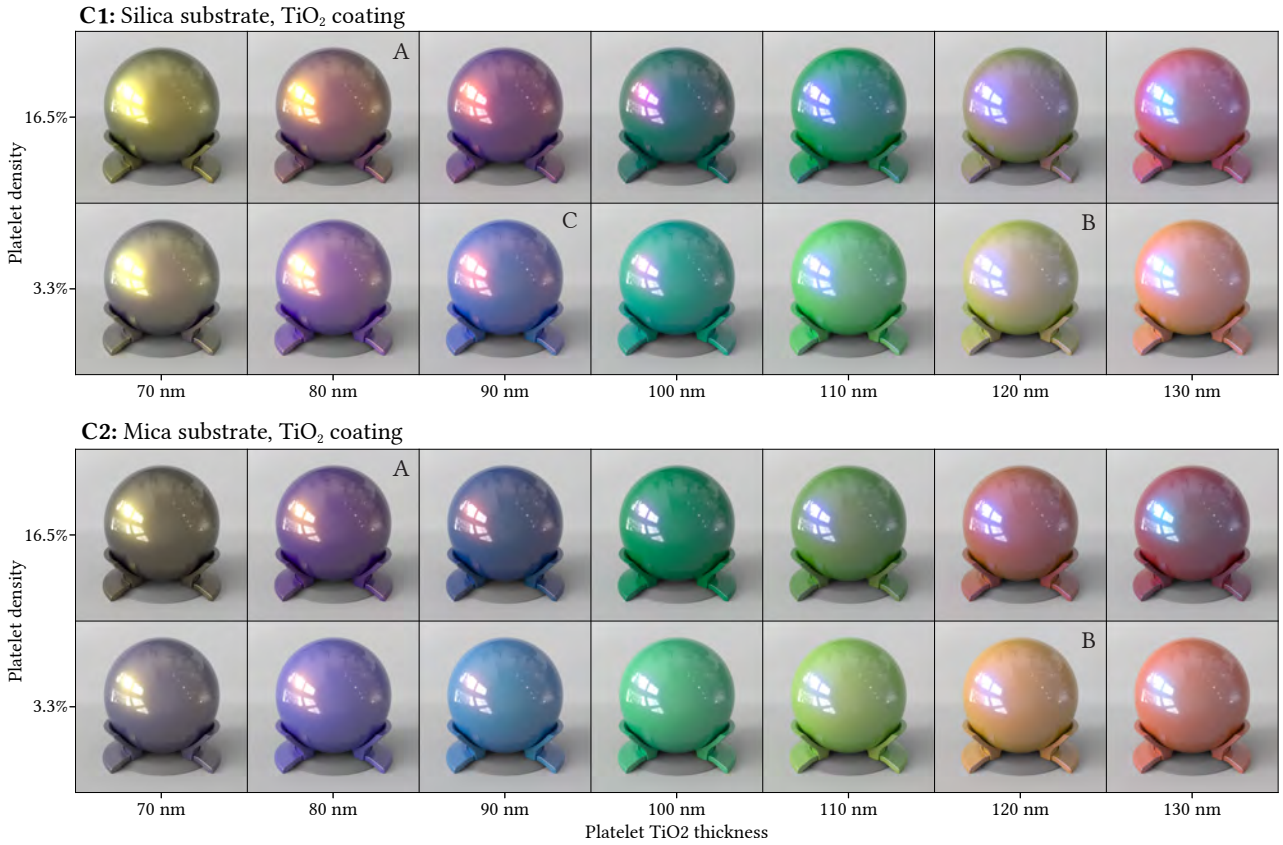

Fig. 11. Variations of pearlescent materials as the thickness of the coating layer and the density of platelets change. **C1 (top)**: Silica substrate ($\tau_s = 80$ with zero deviation), TiO_2 coating. **C2 (bottom):** Mica substrate ($\tau_s = 560.44, \gamma_s = 179.32$). All samples have the same container roughness $\sigma_c = 0.01$, platelet normal deviation $\sigma_p^{xy} = 0.1$, and base stratum albedo $\alpha_b = 0.7$. Changes in the thickness of the coating layer produce large variations in chromaticity. On the other hand, as the density of the platelets increases the diffuse luminance decreases, and the gloss component of the chromaticity progressively dominates the final appearance. While the global behavior is similar with both types of substrate, the resulting appearance is vastly different (see the closeups of samples A and B in Figure 12, right). The material sample highlighted with the letter C (top) illustrates how the gloss hue first manifests around the highlights (please refer to the main text).

and gloss chromaticities change in opposite directions, presenting roughly complementary hues (see pairs of points in Figure 10c).

In addition, as the deviation of the normal distribution σ_p^{xy} increases, multiple scattering becomes dominant. As a consequence, colors become less saturated, both for the diffuse and gloss components (Figure 10d). On the other hand, the platelet density C_p only affects the diffuse component significantly (Figure 10e), especially for small σ_p^{xy}, where the saturation increases with density.

Luminance. Figure 10f shows how diffuse luminance decreases with the platelet density C_p, while the normal distribution deviation σ_p^{xy} has very little effect. Diffuse luminance is also higher on platelets with a thickness between 100 and 130 nm, since coatings in that range yield a higher transmittance (Figures 10g and 10h). The luminance of the gloss component behaves in a complementary manner (Figure 10i).

6.3 Additional results

Figure 11 (top) shows the significant variation in pearlescent appearance that emerges from the interactions of different parameters in our model. In particular, we show appearance changes in our material C1, due to changes in platelet density ρ_p and thickness τ_1 of the TiO_2 coating layer, for a base albedo $\alpha_b = 0.7$. Changes in thickness lead to strong changes in chromaticity, as shown in Figure 10a. On the other hand, as the platelet density C_p increases, the diffuse luminance decreases (as shown in Figure 10h). As a result, the diffuse hue becomes progressively less dominant, and the gloss hue emerges. This gloss hue first manifests subtly around the main highlights produced by the dielectric interface of the container: see for instance the reddish halo around the highlights in the object marked with a C in Figure 11, top; as density increases, this reddish hue progressively dominates the final appearance.

For comparison purposes, we model a second material C2, identical to material C1, except for the substrate; instead of silica, C2 has

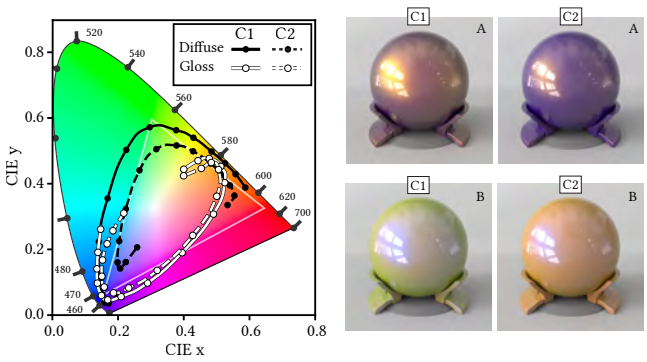

Fig. 12. **Left:** Comparison between the chromaticity of the diffuse (black) and gloss (white) components for the C1 (solid) and C2 (dashed) materials. The different platelet structure results into a different manifold of appearance. **Right:** Side-by-side comparisons of the samples A and B in Figure 11. Despite the large differences in appearance, the only difference in each pair is the substrate material.

a mica substrate, with a mean thickness of 560 nm, and standard deviation 179 nm. It can be seen how changing the substrate has a profound impact on the underlying diffraction phenomena, resulting in a marked shift in overall chrominance (see Figure 11, bottom). This can be better observed in Figure 12, showing closeups of the objects marked with A and B in the previous figure. However, the global behavior of the diffuse and gloss components is essentially equivalent to our previous analysis (Figure 12, left).

In contrast to prior work, our method also admits configurations that lead to an anisotropic BSDF. Figure 13 illustrates changes in appearance due to rotations in the mean direction of the platelets' normals, combined with both isotropic (top) and anisotropic distributions (bottom). We observe that slight rotations in the x axis result in an angular offset between the chromatic gloss produced by platelets and the highlights produced by the roughness of the container.

Table A3 describes the parameters of each material used in Figure 1. Altering a single value per pair of objects, as shown in Figure 1 and highlighted in bold in the table, leads to noticeable appearance changes. Different from previous models, our support for thickness distributions allows us to represent appearance changes (see difference between 7^{th} and 8^{th} bottles in Figure 1) due to variations in substrate thickness, which naturally occur in common substrate compounds such as mica. Finally, Figure 14 demonstrates the generality of our model, showing three different cars rendered with complex pearlescent car paints. We use multi-layer platelets with metallic substrates (front and middle) and alumina substrate (back) [Maile et al. 2005], displaying different degrees of rotation and anisotropy. The exact parameters of each material are described in Table A4.

All renders have been computed on a dual Intel Xeon Gold 6140 using 64 threads. Execution times for all the results in the paper can be found in Table 3. Equal-time comparisons demonstrating the importance of MIS and hero wavelength for efficiently rendering our model can be found in Figure 15.

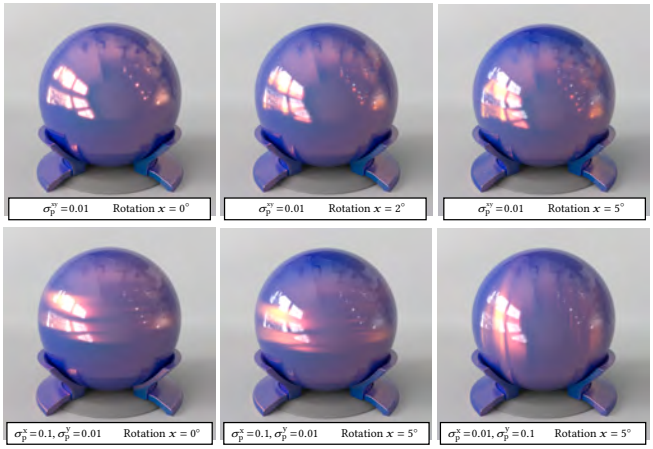

Fig. 13. Variations of material C1 with increasing platelet rotation (shown for the x-axis). Even slight rotations result in a visible angular offset in the highlights produced by the platelets (reddish for this material). **Top:** isotropic normal distributions of the platelets. **Bottom:** anisotropic normal distributions of the platelets. The last image shows anisotropy in the y-axis.

Fig. 14. Cars rendered with complex pearlescent paints, exhibiting platelet rotation and anisotropy. Table A4 describes the parameters of each material.

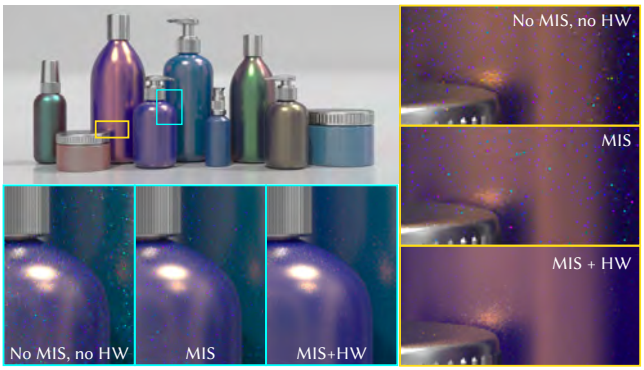

Fig. 15. Equal-time comparisons demonstrating the importance of both multiple importance sampling (MIS) and spectral rendering using hero wavelength (HW), for the scene in Figure 1 rendered at 4K samples per pixel.

Table 3. Total render time, samples per pixel, and resolution for the different scenes used throughout the paper.

Render times

Scene	Time	Samples/pixel	Resolution	Figures
Cosmetics	64 minutes	4k	1600×720	1
Knob	17 minutes	4k	512×512	11, 12, 13
Cars	31 minutes	4k	1280×550	14

7 CONCLUSIONS

We have presented a general model that simulates the complex internal processes responsible for pearlescent appearance, including scattering from multi-layered platelets subject to wave-optical interference, and internal reflection from smooth or rough layer boundaries. Our model is based on a thorough review of the structure and properties of real-world pearlescent pigments, and it accounts for stochastic variation in the local material properties that critically impacts accuracy. We demonstrate the practicality of our method and showcase a series of comparisons that showcase its superior performance compared to prior work. Our results also include an analysis of the influence of physical parameters on the resulting goniochromatic behavior. As this analysis shows, small perturbations of a single parameter often lead to disproportionately large changes in material appearance. We believe that detailed computational mapping of this highly nonlinear space will be a crucial component of future manufacturing application that seek to create pearlescent materials with desired optical properties. To foster future work on this topic, and to ensure the reproducibility of this article, we will release an open implementation of our full simulation pipeline.

Limitations & Future Work. Our model is implemented on top of a spectral renderer. To reduce variance arising from the stochastic nature of transmittance $\widehat{\mathcal{T}}(\omega_i)$ evaluation, the design of efficient sampling methods is an important avenue for future work. While our implementation builds on specialized sampling and MIS techniques for multilayered materials and spectral rendering, it would directly benefit from recent and future advances in both lines of research (e.g. [Gamboa et al. 2020; Xia et al. 2020] and [Kutz et al. 2017]). For applications where rendering efficiency is preferred over exact appearance, faster although less accurate solutions can be employed [Ergun et al. 2016; Ershov et al. 2001], solving the volumetric transport inside the container strata using either precalculated [Jakob et al. 2014a] or approximated solutions [Belcour 2018; Weier and Belcour 2020]. As for the parameter space, our model takes into account the main effects that can be controlled during manufacturing, such as the particular materials used, thickness distributions, or the deviation from the platelet normal distribution. Other manufacturing issues such as irregularities in the substrates, flaws in the layer precipitation process, small thermal and mechanical cracks of the pigments, or discontinuities and pores in the pigments may lead to additional scattering. This potentially replaces iridescence with an undesired hazy appearance, which could be characterized using Mie theory [Maile and Reynders 2003]. To make our model tractable we assume that lateral boundaries of platelets can be ignored. Removal of this approximation could be desirable to further improve accuracy, but this would entail replacing the layering computation by a significantly more costly wave-level simulation that would likely be impractical in the context of rendering. We also assume that all platelets suspended into the material are very small (on the order of a few microns), which is common in many pearlescent materials. Adding larger platelets would allow us to model glints (such as those in many car paints), and would require to replace the continuous distribution of platelets with a discrete counterpart [Jakob et al. 2014b]. Last, while intuitive models for editing BRDFs' appearance exist [Kerr and Pellacini 2010; Serrano et al. 2016], designing tools to enable intuitive editing of pearlescent materials remains a challenging open problem. This will involve translate the physical parameter space into perceptually-based appearance spaces [Lagunas et al. 2019; Pellacini et al. 2000; Wills et al. 2009]. Our model provides a useful foundation, but further work is required to address the high-dimensional and nonlinear nature of the underlying parameter space.

ACKNOWLEDGMENTS

We would like to thank Delio Vicini and Merlin Nimier-David for their assistance while developing the current project on early versions of Mitsuba 2, Manuel Lagunas and Andrea Gregorio for their help with the figures, Alejandro Ferrero for providing the measurements in Section 6.1, Mark Mamak for providing plastic container samples, and Frank Maile for his feedback on pearlescent appearance and manufacturability. This work has been funded by the European Research Council (ERC) under the EU's Horizon 2020 research and innovation programme (project CHAMELEON, Grant no. 682080), DARPA (project REVEAL, HR0011-16-C-0025), and the Spanish Ministerio de Economía y Competitividad (TIN2016-78753-P and PID2019-105004GB-I00).

REFERENCES

Anita I. Bailey and Susan M. Kay. 1965. Measurement of refractive index and dispersion of mica, employing multiple beam interference techniques. *British Journal of Applied Physics* 16, 1 (1965).

Chen Bar, Marina Alterman, Ioannis Gkioulekas, and Anat Levin. 2019. A Monte Carlo Framework for Rendering Speckle Statistics in Scattering Media. *ACM Transactions on Graphics* 38, 4 (2019).

Laurent Belcour. 2018. Efficient rendering of layered materials using an atomic decomposition with statistical operators. *ACM Transactions on Graphics* 37, 4 (2018).

Laurent Belcour and Pascal Barla. 2017. A practical extension to microfacet theory for the modeling of varying iridescence. *ACM Transactions on Graphics* 36, 4 (2017).

Benedikt Bitterli, Srinath Ravichandran, Thomas Müller, Magnus Wrenninge, Jan Novák, Steve Marschner, and Wojciech Jarosz. 2018. A radiative transfer framework for non-exponential media. *ACM Transactions on Graphics* 37, 6 (2018).

Max Born and Emil Wolf. 1999. *Principles of optics: electromagnetic theory of propagation, interference and diffraction of light* (7 ed.). Cambridge University Press.

Brent Burley. 2012. Physically-based shading at Disney. In *Practical physically-based shading in film and game production (Proceedings of ACM SIGGRAPH Courses)*. ACM.

Subrahmanyan Chandrasekhar. 2013. *Radiative transfer*. Dover Publications.

Guy Hubert Stephane Sylvain Culeron, Song Shuo, Ping Wang, Liang Yang, and Chunchuan Liang. 2016. Glossy Container. US Patent Application 2016/0375624 A1.

Tom Cuypers, Tom Haber, Philippe Bekaert, Se Baek Oh, and Ramesh Raskar. 2012. Reflectance Model for Diffraction. *ACM Transactions on Graphics* 31, 5 (2012).

J. R. DeVore. 1951. Refractive Indices of Rutile and Sphalerite. *Journal of the Optical Society of America* 41, 6 (1951).

Zhao Dong, Bruce Walter, Steve Marschner, and Donald P Greenberg. 2015. Predicting appearance from measured microgeometry of metal surfaces. *ACM Transactions on Graphics* 35, 1 (2015).

Craig Donner and Henrik Wann Jensen. 2005. Light diffusion in multi-layered translucent materials. *ACM Transactions on Graphics* 24, 3 (2005).

Serkan Ergun, Sermet Önel, and Aydin Ozturk. 2016. A general micro-flake model for predicting the appearance of car paint. In *Proceedings of the Eurographics Symposium on Rendering: Experimental Ideas & Implementations (EGSR '16)*. Eurographics Association.

Sergey Ershov, Konstantin Kolchin, and Karol Myszkowski. 2001. Rendering pearlescent appearance based on paint-composition modelling. *Computer Graphics Forum* 20, 3 (2001).

Viggo Falster, Adrian Jarabo, and Jeppe Revall Frisvad. 2020. Computing the Bidirectional Scattering of a Microstructure UsingScalar Diffraction Theory and Path Tracing. *Computer Graphics Forum* 39, 7 (2020).

Alejandro Ferrero, Berta Bernad, J Campos, Esther Perales, José Luis Velázquez, and Francisco M Martínez-Verdú. 2016. Color characterization of coatings with diffraction pigments. *Journal of the Optical Society of America A* 33, 10 (2016).

Alejandro Ferrero, Esther Perales, Ana M Rabal, J Campos, Francisco Miguel Martínez-Verdú, Elizabet Chorro, and A Pons. 2014. Color representation and interpretation of special effect coatings. *Journal of the Optical Society of America A* 31, 2 (2014).

Jeppe Revall Frisvad, Niels Jørgen Christensen, and Henrik Wann Jensen. 2007. Computing the scattering properties of participating media using Lorenz-Mie theory. *ACM Transactions on Graphics* 26, 3 (2007).

Luis E. Gamboa, Adrien Gruson, and Derek Nowrouzezahrai. 2020. An Efficient Transport Estimator for Complex Layered Materials. *Computer Graphics Forum* (2020).

Jay S. Gondek, Gary W. Meyer, and Jonathan G. Newman. 1994. Wavelength dependent reflectance functions. In *Proceedings of the 21st Annual Conference on Computer Graphics and Interactive Techniques (SIGGRAPH '94)*. ACM.

Xavier Granier and Wolfgang Heidrich. 2003. A simple layered RGB BRDF model. *Graphical Models* 65, 4 (2003).

Jie Guo, Yanjun Chen, Yanwen Guo, and Jingui Pan. 2018a. A Physically-based Appearance Model for Special Effect Pigments. *Computer Graphics Forum* 37, 4 (2018).

Jie Guo, Jinghui Qian, Yanwen Guo, and Jingui Pan. 2016. Rendering thin transparent layers with extended normal distribution functions. *IEEE Transactions on Visualization and Computer Graphics* 23, 9 (2016).

Yu Guo, Miloš Hašan, and Shuang Zhao. 2018b. Position-Free Monte Carlo Simulation for Arbitrary Layered BSDFs. *ACM Transactions on Graphics* 37, 6 (2018).

Pat Hanrahan and Wolfgang Krueger. 1993. Reflection from layered surfaces due to subsurface scattering. In *Proceedings of the 20th Annual Conference on Computer Graphics and Interactive Techniques (SIGGRAPH '93)*. ACM.

Eric Heitz, Jonathan Dupuy, Cyril Crassin, and Carsten Dachsbacher. 2015. The SGGX microflake distribution. *ACM Transactions on Graphics* 34, 4 (2015).

Hideki Hirayama, Kazufumi Kaneda, Hideo Yamashita, and Yoshimi Monden. 2001. An accurate illumination model for objects coated with multilayer films. *Computers & Graphics* 25, 3 (2001).

Nicolas Holzschuch and Romain Pacanowski. 2017. A two-scale microfacet reflectance model combining reflection and diffraction. *ACM Transactions on Graphics* 36, 4 (2017).

Nagaraj Goud Ireni, Ramanuj Narayan, Pratyay Basak, and K.V.S.N. Raju. 2016. Poly(thiourethane-urethane)-urea as anticorrosion coatings with impressive optical properties. *Polymer* 97 (2016).

Wenzel Jakob, Adam Arbree, Jonathan T Moon, Kavita Bala, and Steve Marschner. 2010. A radiative transfer framework for rendering materials with anisotropic structure. *ACM Transactions on Graphics* 29, 4 (2010).

Wenzel Jakob, Eugene d'Eon, Otto Jakob, and Steve Marschner. 2014a. A comprehensive framework for rendering layered materials. *ACM Transactions on Graphics* 33, 4 (2014).

Wenzel Jakob, Miloš Hašan, Ling-Qi Yan, Jason Lawrence, Ravi Ramamoorthi, and Steve Marschner. 2014b. Discrete stochastic microfacet models. *ACM Transactions on Graphics* 33, 4 (2014).

Adrian Jarabo, Carlos Aliaga, and Diego Gutierrez. 2018. A Radiative Transfer Framework for Spatially-Correlated Materials. *ACM Transactions on Graphics* 37, 4 (2018).

Adrian Jarabo and Victor Arellano. 2018. Bidirectional Rendering of Vector Light Transport. *Computer Graphics Forum* 37, 6 (2018).

William B. Kerr and Fabio Pellacini. 2010. Toward Evaluating Material Design Interface Paradigms for Novice Users. *ACM Transactions on Graphics* 29, 4 (2010).

W. H. Kettler and G. Richter. 1997. Investigation on topology of platelet-like effect-pigments in automotive surface-coatings. *Progress in organic coatings* 31, 4 (1997).

Duck Bong Kim, Myoung Kook Seo, Kang Yeon Kim, and Kwan H Lee. 2010. Acquisition and representation of pearlescent paints using an image-based goniospectrophotometer. *Optical engineering* 49, 4 (2010).

Eric Kirchner. 2009. Film shrinkage and flake orientation. *Progress in Organic Coatings* 65, 3 (2009).

Eric Kirchner and Jacqueline Houweling. 2009. Measuring flake orientation for metallic coatings. *Progress in organic coatings* 64, 2-3 (2009).

Tom Kneiphof, Tim Golla, and Reinhard Klein. 2019. Real-time Image-based Lighting of Microfacet BRDFs with Varying Iridescence. *Computer Graphics Forum* 38, 4 (2019).

Peter Kutz, Ralf Habel, Yining Karl Li, and Jan Novák. 2017. Spectral and Decomposition Tracking for Rendering Heterogeneous Volumes. *ACM Transactions on Graphics* 36, 4 (2017).

Manuel Lagunas, Sandra Malpica, Ana Serrano, Elena Garces, Diego Gutierrez, and Belen Masia. 2019. A Similarity Measure for Material Appearance. *ACM Transactions on Graphics* 38, 4 (2019).

Boris Mahltig, Jieyang Zhang, Linfei Wu, Daniel Darko, Miriam Wendt, Evelyn Lempa, Maike Rabe, and Hajo Haase. 2017. Effect pigments for textile coating: a review of the broad range of advantageous functionalization. *Journal of Coatings Technology and Research* 14, 1 (2017).

Frank J. Maile, Gerhard Pfaff, and Peter Reynders. 2005. Effect pigments—past, present and future. *Progress in organic coatings* 54, 3 (2005).

Frank J. Maile and Peter Reynders. 2003. Substrates for pearlescent pigments. *European coatings journal* 4 (2003).

Irving H. Malitson. 1965. Interspecimen Comparison of the Refractive Index of Fused Silica. *Journal of the Optical Society of America* 55, 10 (1965).

Irving H. Malitson and Marilyn J. Dodge. 1972. Refractive-index and birefringence of synthetic sapphire. *Journal of the Optical Society of America* 62, 11 (1972).

José M. Medina. 2008. Linear basis for metallic and iridescent colors. *Applied optics* 47, 30 (2008).

Bailey Miller, Iliyan Georgiev, and Wojciech Jarosz. 2019. A null-scattering path integral formulation of light transport. *ACM Transactions on Graphics* 38, 4 (2019).

Satoshi Naganawa and Yuta Suzuki. 2016. Modified polysilazane film and method for producing gas barrier film. US Patent 9,512,334.

Merlin Nimier-David, Delio Vicini, Tizian Zeltner, and Wenzel Jakob. 2019. Mitsuba 2: A Retargetable Forward and Inverse Renderer. *ACM Transactions on Graphics* 38, 6 (2019).

Fabio Pellacini, James A. Ferwerda, and Donald P. Greenberg. 2000. Toward a Psychophysically-Based Light Reflection Model for Image Synthesis. In *Proceedings of the 27th Annual Conference on Computer Graphics and Interactive Techniques (SIGGRAPH '00)*. ACM, 55–64.

Gerhard Pfaff. 2003. Special effect pigments based on silica flakes. *Inorganic materials* 39, 2 (2003).

Gerhard Pfaff and Miriam Becker. 2012. Special effect pigments in cosmetics applications. *Household Personal Hold* 7, 1 (2012).

Gerhard Pfaff and Peter Reynders. 1999. Angle-dependent optical effects deriving from submicron structures of films and pigments. *Chemical reviews* 99, 7 (1999).

Petar Pjanic and Roger D Hersch. 2015. Color changing effects with anisotropic halftone prints on metal. *ACM Transactions on Graphics* 34, 6 (2015).

Mikhail N. Polyanskiy. 2020. *Refractive index database.* Retrieved January 1, 2020 from https://refractiveindex.info

Marvin R. Querry. 1985. *Optical constants.* Technical Report CRDC-CR-85034. Missouri University, Kansas City, MO.

Aleksandar D. Rakić. 1995. Algorithm for the determination of intrinsic optical constants of metal films: application to aluminum. *Applied Optics* 34, 22 (1995).

Michael Rösler, Frank J. Maile, and Adalbert Huber. 2008. The macroscopic appearance of effect coatings and its relationship to the local spatial and angular distribution of reflected light. In *Proceedings of American Coating Conference 2008.*

Martin Rump, Gero Müller, Ralf Sarlette, Dirk Koch, and Reinhard Klein. 2008. Photo-realistic rendering of metallic car paint from image-based measurements. *Computer Graphics Forum* 27, 2 (2008).

Szymon M. Rusinkiewicz. 1998. A new change of variables for efficient BRDF representation. In *Rendering techniques' 98*. Springer.

Iman Sadeghi, Adolfo Munoz, Philip Laven, Wojciech Jarosz, Francisco Seron, Diego Gutierrez, and Henrik Wann Jensen. 2012. Physically-based simulation of rainbows. *ACM Transactions on Graphics* 31, 1 (2012).

Ana Serrano, Diego Gutierrez, Karol Myszkowski, Hans-Peter Seidel, and Belen Masia. 2016. An Intuitive Control Space for Material Appearance. *ACM Transactions on Graphics* 35, 6 (2016).

Christopher M. Seubert, Mark E. Nichols, J. Frey, Max Shtein, and Michael D. Thouless. 2016. The characterization and effects of microstructure on the appearance of platelet-polymer composite coatings. *Journal of Materials Science* 51, 5 (2016).

Hiroyuki Shiomi, Eiichirou Misaki, Maoya Adachi, and Fukuji Suzuki. 2008. High chroma pearlescent pigments designed by optical simulation. *Journal of Coatings Technology and Research* 5, 4 (2008).

Brian E. Smits and Gary W. Meyer. 1992. Newton's colors: simulating interference phenomena in realistic image synthesis. In *Photorealism in Computer Graphics*. Springer.

James Speight. 2005. *Lange's Handbook of Chemistry, Sixteenth Edition.* McGraw-Hill Education.

Jos Stam. 1999. Diffraction Shaders. In *Proceedings of the 26th Annual Conference on Computer Graphics and Interactive Techniques (SIGGRAPH '99)*. ACM.

Jos Stam. 2001. An illumination model for a skin layer bounded by rough surfaces. In *Rendering Techniques 2001*. Springer.

Katrin Steinbach and Ulrich Schmidt. 2010. Borosilicate Pigments–Transparency Meets Brilliance and Sparkle. *Cosmetic Science Technology* 2010 (2010).

Shlomi Steinberg. 2019. Analytic Spectral Integration of Birefringence-Induced Iridescence. *Computer Graphics Forum* 38, 4 (2019).

Yinlong Sun. 2006. Rendering Biological Iridescences with RGB-Based Renderers. *ACM Transactions on Graphics* 25, 1 (2006).

Yinlong Sun and Qiqi Wang. 2008. Interference shaders of thin films. *Computer Graphics Forum* 27, 6 (2008).

Antoine Toisoul and Abhijeet Ghosh. 2017. Practical acquisition and rendering of diffraction effects in surface reflectance. *ACM Transactions on Graphics* 36, 5 (2017).

Ping Wang, Liang Yang, John Andrew McDaniel, Gian Armand Juliana DeBelder, and Gaoyang Wang. 2014. Pearlescent container. US Patent 8,859,067 B2.

Andrea Weidlich and Alexander Wilkie. 2007. Arbitrarily layered micro-facet surfaces. In *Proceedings of the 5th international conference on Computer graphics and interactive techniques in Australia and Southeast Asia (GRAPHITE '07)*. ACM.

Philippe Weier and Laurent Belcour. 2020. Rendering Layered Materials with Anisotropic Interfaces. *Journal of Computer Graphics Techniques (JCGT)* 9, 2 (2020), 37–57.

Sebastian Werner, Zdravko Velinov, Wenzel Jakob, and Matthias B. Hullin. 2017. Scratch Iridescence: Wave-optical Rendering of Diffractive Surface Structure. *ACM Transactions on Graphics* 36, 6 (2017).
Alexander Wilkie, Sehara Nawaz, Marc Droske, Andrea Weidlich, and Johannes Hanika. 2014. Hero Wavelength Spectral Sampling. *Computer Graphics Forum* 33, 4 (2014).
Josh Wills, Sameer Agarwal, David Kriegman, and Serge Belongie. 2009. Toward a Perceptual Space for Gloss. *ACM Transactions on Graphics* 28, 4 (2009).
Mengqi Xia, Bruce Walter, Christophe Hery, and Steve Marschner. 2020. Gaussian Product Sampling for Rendering Layered Materials. *Computer Graphics Forum* 39, 1 (2020).
Tomoya Yamaguchi, Tatsuya Yatagawa, Yusuke Tokuyoshi, and Shigeo Morishima. 2019. Real-time Rendering of Layered Materials with Anisotropic Normal Distributions. In *SIGGRAPH Asia 2019, Technical Briefs*. ACM.
Ling-Qi Yan, Miloš Hašan, Bruce Walter, Steve Marschner, and Ravi Ramamoorthi. 2018. Rendering specular microgeometry with wave optics. *ACM Transactions on Graphics* 37, 4 (2018).
Pochi Yeh. 1988. *Optical waves in layered media.* John Wiley & Sons, Ltd.
Tizian Zeltner and Wenzel Jakob. 2018. The layer laboratory: a calculus for additive and subtractive composition of anisotropic surface reflectance. *ACM Transactions on Graphics* 37, 4 (2018).
Shuang Zhao, Wenzel Jakob, Steve Marschner, and Kavita Bala. 2011. Building volumetric appearance models of fabric using micro CT imaging. *ACM Transactions on Graphics* 30, 4 (2011).

A TABLES

In the following we describe the characteristics of container, substrate, and coating compounds used throughout the paper. Please also refer to Table 1 for a description of the symbols.

Table A1. Characterization of the materials used throughout the paper [Polyanskiy 2020]. For transparent materials, we report the measured index of refraction η and Abbe number V_d. For absorbing materials (Fe_2O_3, aluminum and copper) we report the average η from measured data. In the case of PET an polysilazane there are no accurate measurements and we resort to a constant η.

Material	η	V_d	**Source**
Air	1.0		
PET	1.5750		[Speight 2005]
Polyurethane	1.5650	24.37	[Ireni et al. 2016]
Polysilazane	1.5550		[Naganawa and Suzuki 2016]
Mica	1.6137	54.56	[Bailey and Kay 1965]
SiO_2	1.4585	67.82	[Malitson 1965]
TiO_2	2.6142	9.87	[DeVore 1951]
Fe_2O_3	$3.3206 + 0.2192i$		[Querry 1985]
Al_2O_3	1.7742	72.31	[Malitson and Dodge 1972]
Al	$1.1978 + 7.0488i$		[Rakić 1995]
Cu	$0.7400 + 2.7071i$		[Querry 1985]

Table A2. Optimized parameters for our model and Ergun's [2016] (see Figure 6 and Figure 7 in the main text).

Material	**Model**	$\rho_\mathbf{p}$	$\tau_\mathbf{s}$ (nm)	$\gamma_\mathbf{s}$	τ_1 (nm)	$\sigma_\mathbf{p}^\mathbf{xy}$
MCS1	[Ergun et al. 2016]	6.6%	160	0	120	0.1
	Ours	3.3%	280	40	60	0.1
MCS2	[Ergun et al. 2016]	13.2%	400	0	60	0.1
	Ours	13.2%	410	40	60	0.1
BFS1	[Ergun et al. 2016]	13.2%	160	0	60	0.1
	Ours	13.2%	160	20	60	0.1

Table A3. Description of the parameters used to render the objects in Figure 1 (bottles numbered in reading order), where C_p is the platelet density (fraction of platelets per total volume), τ_1 is the TiO_2 thickness, $\sigma_\mathrm{p}^\mathrm{xy}$ is the deviation of the mean normal, σ_c is the dielectric roughness, γ_s is the deviation of the substrate thickness. We highlight in bold the varying parameter for each pair. All materials have base stratum albedo $\alpha_\mathrm{b} = 0.6$, and a PET container.

Bottles: Materials Description

Bottle	$C_\mathbf{p}$	τ_1 **(nm)**	$\sigma_\mathbf{p}^\mathbf{xy}$	$\sigma_\mathbf{c}$	γ_s	**Substrate**
1	**13.2%**	140	0.05	0.2	179.32	Mica
2	**1.3%**	140	0.05	0.2	179.32	Mica
3	9.9%	85	0.02	0.1	**0.0**	**SiO_2**
4	9.9%	85	0.02	0.1	**179.32**	**Mica**
5	6.6%	90	**0.01**	0.1	179.32	Mica
6	6.6%	90	**0.2**	0.1	179.32	Mica
7	6.6%	70	0.07	0.07	**22.41**	Mica
8	6.6%	70	0.07	0.07	**179.32**	Mica
9	2.0%	90	0.05	0.02	179.32	Mica

Table A4. Description of the parameters used to render the cars in Figure 14. Front and middle cars have double-coating metallic platelets, and back car single-coating Alumina platelets [Maile et al. 2005].

Cars: Materials Description

Car	**Front**	**Middle**	**Back**
Coating 1	TiO_2 (147 nm)	TiO_2 (70 nm)	TiO_2 (80 nm)
Coating 2	Fe_2O_3 (80 nm)	Fe_2O_3 (115 nm)	—
Substrate	Cu (80 nm)	Al (80 nm)	Al_2O_3 (40 nm)
$\sigma_\mathrm{p}^\mathrm{xy}$	$(0.05, 0.1)$	$(0.1, 0.01)$	$(0.02, 0.1)$
Rotation (x,y,z)	$(10°, 0°, 0°)$	$(10°, 0°, 0°)$	$(5°, -3°, 0°)$
C_p	6.6%	6.6%	6.6%
σ_c	0.1	0.01	0.05
α_b	0.5	0.7	0.3